Wind tunnel testing of the DeepWind demonstrator in design and tilted operating conditions

L. Battisti [a], E. Benini [a], A. Brighenti [a], M. Raciti Castelli [a, *], S. Dell'Anna [a], V. Dossena [b], G. Persico [b], U. Schmidt Paulsen [c], T.F. Pedersen [c]

[a] *Laboratorio interdisciplinare di Tecnologie Energetiche, Dipartimento di Ingegneria Civile, Ambientale e Meccanica, Università di Trento, Via Mesiano 77, I-38123 Trento, Italy*

[b] *Laboratorio di Fluidodinamica delle Macchine, Dipartimento di Energia, Politecnico di Milano, Via Lambruschini 4, I-20158 Milano, Italy*

[c] *Department of Wind Energy, Technical University of Denmark, Risø Campus, Frederiksborgvej 399, DK-4000 Roskilde, Denmark*

The DeepWind Project aims at investigating the feasibility of a new floating vertical-axis wind turbine (VAWT) concept, whose purpose is to exploit wind resources at deep-water offshore sites.

The results of an extensive experimental campaign on the DeepWind reduced scale demonstrator are here presented for different wind speeds and rotor angular velocities, including also skewed flow operation due to a tilted rotor arrangement. To accomplish this, after being instrumented to measure aerodynamic power and thrust (both in streamwise and transversal directions), a troposkien three-bladed rotor was installed on a high precision test bench, whose axis was suitable to be inclined up to 15° with respect to the design (i.e. upright) operating condition.

The experiments were performed at the large scale, high speed wind tunnel of the Politecnico di Milano (Italy), using a "free jet" (open channel) configuration. The velocity field in the wake of the rotor was also fully characterized by means of an instrumented traversing system, to investigate the flow distribution downstream of the test section.

Special care is taken in the description of the experimental set-up and of the measured data, so that the present results can be used as a benchmark for the validation of simulation models.

1. Introduction

From early experiments [1] to their current status as mature supplier of carbon-free energy, commercial wind turbine generators have grown from nearly 50 kW to over 6 MW [2,3] (with projects under development for 10 MW [3,4]). In fact, even though incremental improvements in the power output have continuously been sought through the aerodynamic optimization of rotor blade design [5,6], it has been definitively accepted that major gains in rated power can only be achieved by increasing the swept area of the rotor [7]. Hence, a massive rise in the dimension of high-scale wind turbines has been registered during the last 30 years, up to well over 100 m diameters [3,8,9].

On the other hand, locating wind turbines on high potential sites will be necessary for future sustained growth [10], the influence of the wind speed being even more pronounced with respect to that of rotor diameter, due to the well-known cubic relation between freestream wind velocity and turbine power output [11]. And this is actually why offshore wind power has become firmly established as a mainstream electricity source, thanks to higher wind speeds and less competition for space with respect to land based wind farms [12–14].

Nevertheless, although the prospects for such installations are promising in the long term, the technology faces a number of challenges, such as the exploitation of wind resources at deep-water offshore sites (i.e. water depths greater than 60 m [15]), where traditional fixed-base designs are no more economically feasible. To get around this problem, floating platforms for offshore wind turbines have been conceived starting from the early 70s [16] and nowadays appear definitively competitive in terms of levelized cost of energy (LCoE) with respect to traditional sub-sea foundations [17].

So far, offshore wind energy conversion systems have relied on

Article history:
Received 7 October 2015
Received in revised form
15 May 2016
Accepted 21 May 2016

Keywords:
VAWT
DeepWind project
Troposkien rotor
Skewed flow
Wind tunnel measurements
Wind turbine benchmark data

* Corresponding author.
E-mail address: marco.raciticastelli@unitn.it (M. Raciti Castelli).

Published Journal Article available at: http://dx.doi.org/10.1016/j.energy.2016.05.080

conventional three-bladed horizontal-axis wind turbines (HAWTs): as a matter of fact, even though extensive research programs on Darrieus rotors were undertaken in the late 70s/early 80s [18–23], any attempts to replace common HAWTs with alternative configurations failed. Nevertheless, the set-up of vertical-axis wind turbines (VAWTs) may provide key advantages in off-shore configurations, by allowing to place the (heavy) generator (and the related components) at the base of the tower; this lowers the topside centre of gravity, thus reducing the platform stability requirements (for a detailed analysis of the potential balance-of-station cost savings due to a reduced platform size, the reader is referred to [24–26]).

Several novel configurations for floating VAWTs have been proposed recently [27–33]. In this scenario, the FP7 European granted DeepWind Project appears as the most radical departure in wind turbine design for 30 years to date, combining a high-scale (5 MW, even though a further potential increment up to 20 MW is under consideration) troposkien-shaped VAWT with a floating platform as a foundation, encompassing a direct drive subsea generator [27–30]. Furthermore, the DeepWind concept was introduced at a time (2010) when important emerging technologies (such as floating spar buoy and mooring system, direct drive subsea generator, highly-controlled pultrusion process for blade manufacturing) were addressed and were integrated into its design with the aim of obtaining a less expensive turbine than conventional competitors.

A crucial design requirement of the DeepWind concept is the limitation of heel angle within 14° [31]; even though the floating platform implements the spar technology [32] and the low centre of gravity guarantees a large overdriving moment, the rotor is expected to tilt during operation, acting as a gyro and describing an elliptical trajectory on the water plane [33]. Such issue raises several concerns about the aerodynamic behaviour of the turbine, prompting for further investigations aiming at a deeper comprehension of skewed flow VAWT operation due to a tilted rotor arrangement.

In the present study, a scaled model of the DeepWind turbine is tested by resorting to dedicated wind tunnel experiments in both upright and tilted configurations, to investigate the turbine performance and to quantify the impact of a 15° tilting, as extreme rotor tilt angle. The paper is structured as follows: after a Literature survey, the turbine model and the experimental set-up are described in detail; then the results are presented in terms of force/power exchange, turbine overall performance and wake flow field for both upright and tilted configurations.

2. Literature survey of VAWT experiments in skewed flow

As an emerging research field related to offshore semi-submersible installations, there are little to no historical data on tilted VAWT operation, except for the computational study of Wang et al. [34], who proposed some modifications to the well-known double multiple streamtube model [35,36] with the aim of simulating the behaviour of a tilted rotor.

Nevertheless, even though the simplification of a tilted VAWT in a skewed flow does not fully model the actual operation in the urban condition (rotors operating on flat rooftops), relevant information can be derived from studies on small-scale VAWTs operating within the built environment. Far from being just foundations, buildings may play an active role in increasing the turbine conversion rate, which can profit from the local flow acceleration due to boundary layer separation at the windward roof edge [37]; furthermore, the velocity vector on top of high-rise buildings is skewed by 10° to 20° with respect to the horizontal [37], a value close to the maximum predicted tilt angle (15°) of the DeepWind rotor during operation.

Operation of VAWTs in skewed flow conditions has been experimentally investigated on building augmented wind turbines (BAWTs) [37–39], which feature machines installed on the flat roof on top of mid-to high-rise buildings. Mertens et al. [37] performed experiments on a two-bladed H-Darrieus turbine both in horizontal and skewed flow, registering an increase (close to 30%) in the aerodynamic performance for skew angles between 20° and 30°. This result was explained by resorting to the three-dimensional architecture of the H-Darrieus layout, which leads to an increase of the energy extracting area in skewed flow. Further investigations, using a blade element - momentum (BEM) approach, suggest that the local induction factors might rise above 0.5 in skewed conditions, requiring the implementation of empirical corrections (see Ref. [7]) on the thrust force to overcome the breakdown of momentum theory. Presently such relations are still not known for skewed flows, calling for the experimental determination of the thrust on tilted rotor blades to calibrate BEM codes.

Ferreira et al. [40,41] investigated the behaviour of a couple of two-bladed H-Darrieus rotors, in both non-skewed and skewed flow, by measuring the aerodynamic thrust and assuming the torque to vary with the same tendency (see also [42]). Velocity measurements with particle image velocimetry and hot wires, performed by the same authors, confirmed that additional aerodynamic power is obtained in skewed flow conditions, and suggested that such extra-power is achieved during the rear portion of the revolution, in the area which is not shadowed by the wake generated during the upwind blade passage.

Using a vorticity transport model, Scheurich and Brown [43] numerically simulated the aerodynamic performance and wake dynamics of different VAWT architectures in both non-skewed and skewed flow, arguing a skewed convection of the wake during oblique flow operation, thereby allowing a portion of each blade to operate entirely in unperturbed conditions. As a consequence, an increased power production was obtained, especially at higher tip speed ratios, since skewed flow caused the vortical structures in the wake to be swept efficiently away from the rotational blade trajectory.

Table 1 shows a summary of the aforementioned extensive wind tunnel campaigns conducted on VAWTs operating in skewed flow: a certain lack of experimental data is readily seen, calling for a simultaneous measurement of power and thrust, thus allowing the validation of numerical codes based on the BEM approach, as well as the measurement of wake velocities, which can help the calibration of both CFD and vortex methods. Moreover, it is worth noting that research on rotor aerodynamics and performance behaviour of a troposkien VAWT in skewed flow still remains a challenge. The present experimental campaign aims at filling this gap through a simultaneous measurement of aerodynamic power and thrust (both in streamwise and transversal directions), while providing a full characterization of the velocity and turbulence field in the rotor wake.

3. Methodology

3.1. The DeepWind demonstrator

To support the development of the DeepWind project, a 1 kW

Table 1
Summary of the main experimental campaigns conducted on VAWTs operating in skewed flow and comparison with the hereby proposed measurements.

Ref.	Year	Rotor power	Rotor thrust	Flow measurement
[37]	2003	Yes	No	No
[40]	2006	No	Yes	Yes
[41]	2009	No	No	Yes
Present work	2015	Yes	Yes	Yes

demonstrator was manufactured, aimed at exploring some crucial technological and operational aspects. Table 2 summarises the main geometric features and inertial properties of the rotor, characterized by three glass fibre blades (laid up over a central foam core, see Ref. [44]) extending from hub to hub, see Fig. 1. To provide future computational investigations with a complete set of information about rotor blade modelling, Table 3 summarises the planform geometry of the blade longitudinal axis (visible in Fig. 1, placed in c/4 along the chord line and in half thickness of the blade), deriving from an ideal troposkien shape (due to the small rotor size, the effect of gravity was considered negligible with respect to centrifugal forces caused by rotation), characterized by a height/diameter ratio $\beta = H/2R_{eq} = 0.97$, which is typical of troposkien architectures: see Ref. [18] ($\beta = H/2R_{eq} = 0.98$) and [21] ($\beta = H/2R_{eq} = 1.02$) for similar rotors from the literature, while for further details about the ideal troposkien geometry (where $\beta = H/2R_{eq} = 0.99$) see Ref. [45,46]).

3.2. Description of the experimental set-up

The present experimental campaign was conducted at the Politecnico di Milano (IT) large scale - high speed wind tunnel. It consists of a closed-loop facility with a working section of 4.00 *m* width, 3.84 *m* height and 6.00 *m* length, where up to 55 *m/s* wind speeds can be provided by means of two arrays of multiple fans working in parallel.

Considering the dimension of the turbine with respect to that of the chamber (the solid blockage, defined as the ratio between the frontal rotor area and that of the wind tunnel, would have exceed 17%) the hereby proposed measurements were performed using a "free jet" (open) configuration. Such a layout was obtained by removing the test room (upstream the diffuser leading to the arrays of fans) and positioning the rotor directly facing the upstream tunnel. High flow quality was assured by a combination of honeycombs and anti-turbulence screens, with a measured freestream turbulence intensity (at the inlet of the open test section) lower than 1%. Fig. 2 illustrates a side view of the open chamber, showing also the DeepWind demonstrator rotor during both design (upright) and tilted operation; a dimensional scheme of the experimental facility and rotor set up is also reported in Fig. 3.

Even though tests were performed in free-jet configuration, the relatively high solid blockage (raising to 18.4% by including the upper part of the hull in the frontal turbine area) might affect the present experiments. Therefore a quantification was performed to estimate the impact of free-jet blockage in the present

Table 2
Main geometric features and mass properties of the DeepWind demonstrator rotor.

Blade profile	DU-06-W200
R_{eq} [m]	1.014
H [m]	1.902
Rotational direction	Anticlockwise
A_s [m^2]	2.63
t [m]	0.020
c [m]	0.101
σ [−]	0.310
Blade attachment point*	c/4
D_{pole} [m]	0.150
H_{pole} [m]	2.055
t_{flange} [m]	0.010
d_{flange} [m]	0.170
D_{flange} [m]	0.246
M [kg]	27
I_z [kgm^2]	3.8

* Along the chord line.

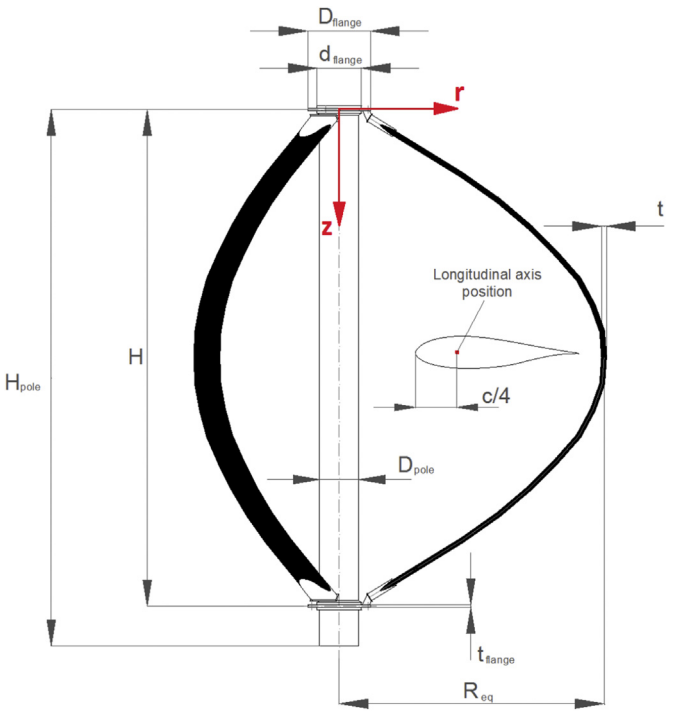

Fig. 1. Quoted drawing of the DeepWind demonstrator for wind tunnel testing; a quoted drawing (out of scale) of the blade section is also shown, evidencing the position of the blade longitudinal axis and its cylindrical coordinates (r,z) collected in Table 3.

configuration; Merker and Wiedemann developed a model to estimate the open-jet blockage of non rotating bluff bodies [47], which is now applied in the formulation adapted and proposed in Ref. [48]. According to the model, a blockage correction coefficient is defined as the ratio between the open-field wind speed (V'_∞) and the open-jet wind speed (V_∞) that induces the same forces on the turbine blades; this correction can be expressed as the sum of three contributions:

$$\frac{V'_\infty}{V_\infty} = 1 + \varepsilon_S + \varepsilon_N + \varepsilon_C \tag{1}$$

which are defined and quantified as follows:

- jet expansion induced velocity coefficient around the body $\varepsilon_S = -0.0026$,
- nozzle induced velocity coefficient due to the model position $\varepsilon_N = 0.0047$,
- collector induced velocity coefficient due to the model position $\varepsilon_C = 0.0295$.

Even though some contributions have different signs, the global blockage correction coefficient is positive and amounts to about 3.2%, meaning that a few percent lower wind speed would be required in the present tests to recover the open field configuration. However, such correction is quantitatively very small (probably comparable to the uncertainty of the model itself, which is here applied in a different context with respect to that of its original conception) and its impact on thrust and power would be even smaller, hence no blockage correction was applied to the present data.

3.2.1. Test bench instrumentation

Rotor torque and thrust measurements were performed using a

Table 3
Cylindrical coordinates of rotor blade longitudinal axis along 101 blade sections, according to Fig. 1. The longitudinal axis is placed in c/4 along the chord line and in half thickness of the blade.

Station [−]	*r* [m]	*z* [m]	*Station* [−]	*r* [m]	*z* [m]	*Station* [−]	*r* [m]	*z* [m]	*Station* [−]	*r* [m]	*z* [m]
1	0.0000	0.9800	26	0.2534	0.8389	51	0.5069	0.6838	76	0.7603	0.4877
2	0.0101	0.9744	27	0.2636	0.8331	52	0.5170	0.6770	77	0.7704	0.4781
3	0.0203	0.9689	28	0.2737	0.8272	53	0.5271	0.6702	78	0.7805	0.4683
4	0.0304	0.9633	29	0.2838	0.8213	54	0.5373	0.6633	79	0.7907	0.4583
5	0.0405	0.9577	30	0.2940	0.8155	55	0.5474	0.6563	80	0.8008	0.4481
6	0.0507	0.9522	31	0.3041	0.8095	56	0.5575	0.6493	81	0.8110	0.4376
7	0.0608	0.9466	32	0.3142	0.8036	57	0.5677	0.6421	82	0.8211	0.4268
8	0.0710	0.9410	33	0.3244	0.7976	58	0.5778	0.6350	83	0.8312	0.4157
9	0.0811	0.9354	34	0.3345	0.7916	59	0.5879	0.6277	84	0.8414	0.4043
10	0.0912	0.9298	35	0.3447	0.7856	60	0.5981	0.6203	85	0.8515	0.3925
11	0.1014	0.9242	36	0.3548	0.7795	61	0.6082	0.6129	86	0.8616	0.3803
12	0.1115	0.9186	37	0.3649	0.7734	62	0.6184	0.6054	87	0.8718	0.3677
13	0.1216	0.913	38	0.3751	0.7673	63	0.6285	0.5978	88	0.8819	0.3547
14	0.1318	0.9074	39	0.3852	0.7611	64	0.6386	0.5900	89	0.8921	0.3410
15	0.1419	0.9018	40	0.3953	0.7549	65	0.6488	0.5822	90	0.9022	0.3268
16	0.1521	0.8961	41	0.4055	0.7487	66	0.6589	0.5743	91	0.9123	0.3119
17	0.1622	0.8905	42	0.4156	0.7424	67	0.6690	0.5663	92	0.9225	0.2961
18	0.1723	0.8848	43	0.4258	0.7361	68	0.6792	0.5581	93	0.9326	0.2795
19	0.1825	0.8791	44	0.4359	0.7297	69	0.6893	0.5498	94	0.9427	0.2617
20	0.1926	0.8734	45	0.4460	0.7233	70	0.6995	0.5414	95	0.9529	0.2425
21	0.2027	0.8677	46	0.4562	0.7168	71	0.7096	0.5328	96	0.9630	0.2216
22	0.2129	0.8620	47	0.4663	0.7103	72	0.7197	0.5241	97	0.9732	0.1984
23	0.2230	0.8562	48	0.4764	0.7038	73	0.7299	0.5153	98	0.9833	0.1720
24	0.2332	0.8505	49	0.4866	0.6972	74	0.7400	0.5063	99	0.9934	0.1406
25	0.2433	0.8447	50	0.4967	0.6905	75	0.7501	0.4971	100	1.0036	0.0995
									101	1.0137	0.0000

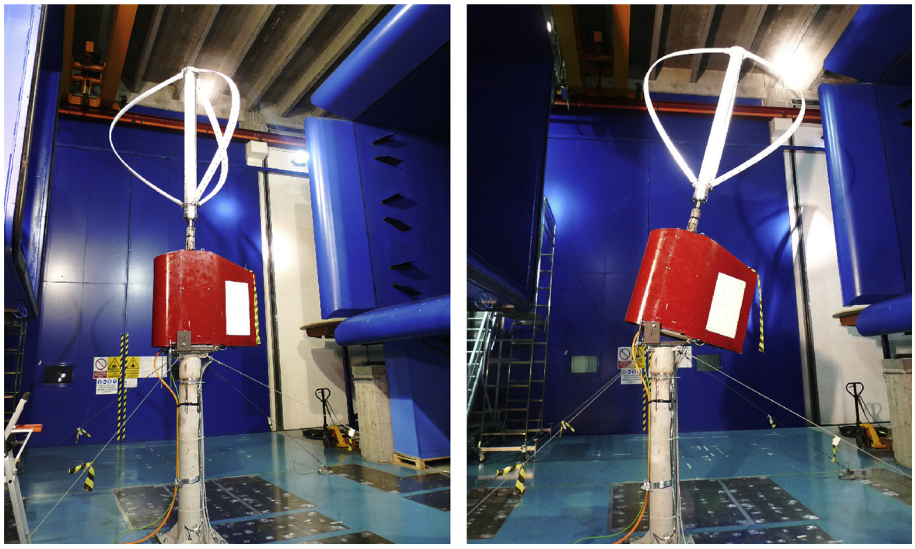

Fig. 2. Side view of the Politecnico di Milano open chamber, showing also the tested rotor arrangement for both design (left) and tilted (right) operating conditions.

high precision test bench (see Fig. 4 and Table 4), which was instrumented on a shaft below the lowest blade support, using the following calibrated sensors:

- 2 *strain gauge bridges*, installed on the supporting mast, to measure both streamwise and transversal aerodynamic thrusts;
- an *absolute encoder*, to provide both rotational speed and rotor phase (i.e. the azimuthal position of the reference blade);
- a precision *torquemeter* to measure the mechanical torque at rotor shaft.

The main characteristics of the measurement sensors are reported in Table 4. An 8-poles synchronous motor/generator with a rated power of 8.6 kW was mounted on the power train (see Fig. 4) and controlled by an inverter to guarantee constant rotational speed during the tests. Data were acquired by a Compact-RIO device (National Instruments, NI cRIO-9082). A sampling and logging frequency of 2000 Hz was adopted, that is 133 times (at 300 rpm) and 200 times (at 200 rpm) faster than the 3P aerodynamic frequency of the VAWT. While instantaneous (local) aerodynamic data were registered as a function of time, averaged torque and thrust were obtained registering 3 min time series for each rotor operating condition. The interested reader is referred to [48] for mode details about the data acquisition and data

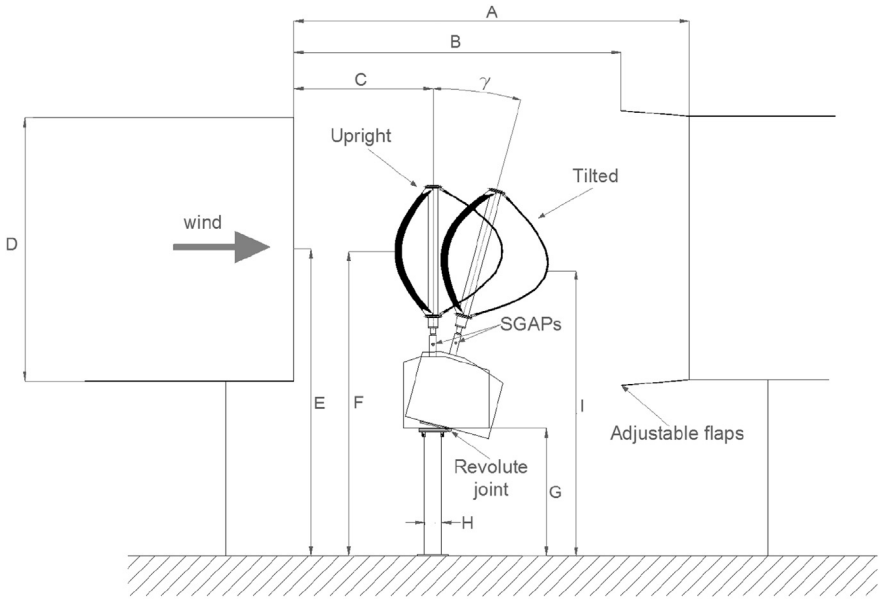

A [mm]	B [mm]	C [mm]	D [mm]	E [mm]	F [mm]	G [mm]	H [mm]	I [mm]	γ [°]
5800	4800	2040	3840	4500	4466	1870	250	4175	15

Fig. 3. Scheme of the experimental facility and rotor set up. As in Fig. 4, the strain gauges application points (SGAPs) are represented, both in upright and tilted operating conditions.

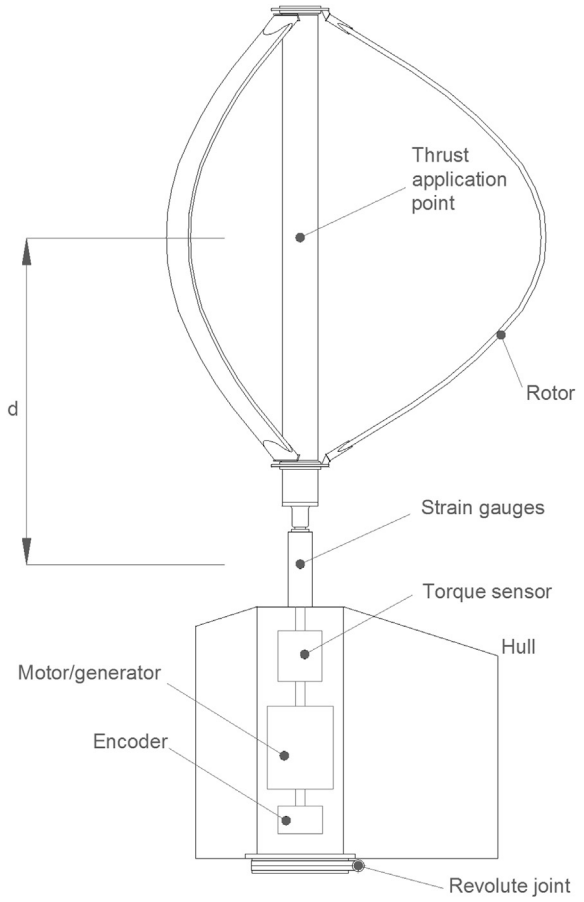

Fig. 4. Schematic diagram of the test bench instrumentation, showing the thrust application point and its distance d from the strain gauges.

processing techniques.

An aerodynamically-shaped hull was positioned around the measurement train. Fig. 5 shows both plan and side views of the hull, thus providing future computational studies with a complete modelling of the experimental set up.

3.2.2. Traversing system

Wake measurements were performed in a vertical $Y_{WM} - Z_{WM}$ plane, located 1.5 diameters downstream of the rotor test section, and two computer-controlled measurement systems (see Fig. 6) were adopted to measure the time averaged and time-resolved flow field:

- a directional *pneumatic five hole probe*, capable of measuring the time-averaged pressure field and the 3D velocity vector. The probe was calibrated on a low speed jet over an angular range of $\pm 24^\circ$ for the yaw angle, i.e. the one between the horizontal (Y_{WM}) and the streamwise (X_{WM}) velocity components, and of $\pm 12^\circ$ for the pitch angle, i.e. the one between the vertical (Z_{WM}) and the streamwise (X_{WM}) velocity components. Uncertainty in pressure measurements resulted lower than 5 Pa, while an uncertainty of 0.2° was evaluated for flow angle measurements;
- two single sensor *hot wire anemometers*, characterized by 5 μm diameter sensor wires, operated in constant temperature mode. One of the hot wire probes was mounted vertically and was rotated in multiple angular positions to achieve, via directional calibration, the time-resolved measurements of velocity magnitude and horizontal flow angle. The second hot wire probe was mounted in streamwise direction, so to achieve a direct velocity measurement avoiding any specific directional calibration. Uncertainty in the velocity measurement resulted about 2% after calibration in a low-speed jet. The turbulence intensity (based on turbulent velocity component in streamwise direction) was also extracted by time-resolved hot wire measurements.

Table 4
Main characteristics of the data acquisition system.

Signal output	Sensor type	Sensor range	Sensor accuracy
Tower bending moment orthogonal to the spinning axis	Strain gauges Full bridge	±250 Nm	±1.5 Nm
Shaft torque	Torque meter	±200 Nm	±0.1 Nm
Rotational speed	Absolute encoder	6000 rpm	±0.04 rad/s
Blades azimuthal position	Absolute encoder	Full range	+1.8° (200 rpm) +3.6° (400 rpm)
Air temperature	RTD PT 100	From −196 °C to 300 °C	±0.012 °C
Air pressure	Barometer	From 800 hPa to 1060 hPa	±1 hPa

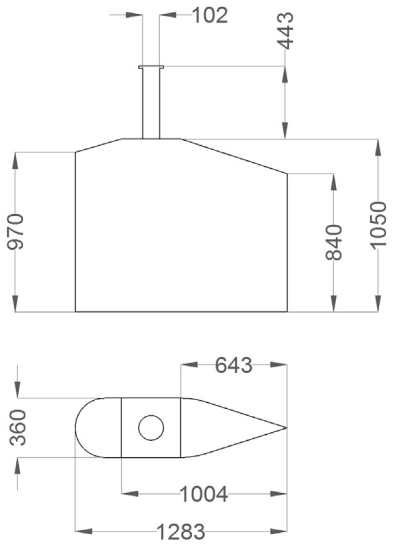

Fig. 5. Quoted drawing of the hull (dimensions in [mm]).

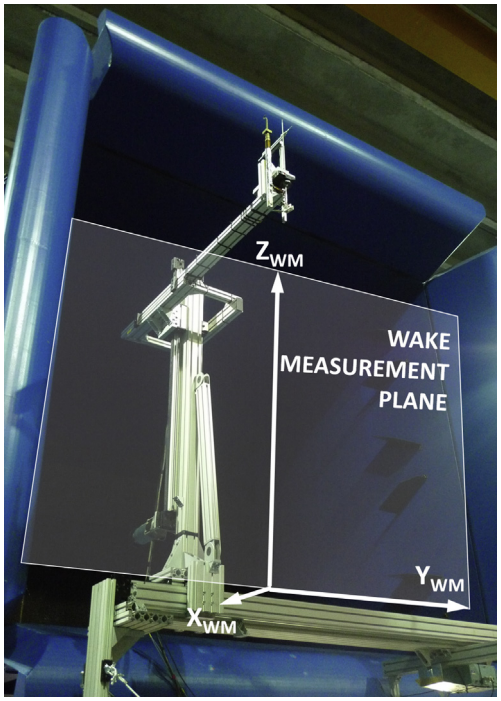

Fig. 6. Motorized sensor arrangement on the traversing system downstream of rotor test section and representation of the wake measurement plane.

The sensors were traversed on a measurement grid of $y \times z = 3290\ mm \times 966\ mm$, defined by 23 points along the horizontal (Y_{WM}) direction and 10 points along the vertical (Z_{WM}) one, extending from rotor equatorial plane ($z/H = 0.5$) to its lower blade tip ($z/H = 0$). The grid was tapered towards the blade tip, to guarantee a proper spatial resolution where a narrower wake is shed by the troposkien rotor.

3.3. Test scheduling and data reduction

The proposed measurements were mainly performed at two constant nominal angular velocities Ω_n (200 *rpm* and 300 *rpm*), varying the freestream wind velocity V_∞ from a minimum value of nearly 4 *m/s* to a maximum one of nearly 15 *m/s*.

The data acquisition system provided rough data, converted from voltage or current to derived quantities, such as bending moment, mechanical torque and rotational speed. A further data processing was performed to obtain other quantities, such as gross aerodynamic torque, power and rotor thrust (T), here assumed as acting at rotor midspan (located at $d = 1.435$ m from the sensors, as shown in Fig. 4) and derived from the bending moment (M_T) provided by the strain gauges. Generally speaking:

$$T = \frac{M_T}{d} = \frac{A\delta + B}{d} \tag{2}$$

where δ is the strain gauge full bridge signal, A and B are the sensor calibration coefficients.

Even though the aerodynamic torque coefficient, defined as:

$$C_Q = \frac{Q_{aero}}{0.5\rho A_s R V_\infty^2} \tag{3}$$

is usually adopted as a dimensionless performance parameter in the aerodynamics of wind turbines, in the present work dimensional aerodynamic torque data are presented in order to facilitate the comparison with performance prediction models. Nevertheless, to provide a complete dataset of the measurement campaign, also torque coefficient data are provided in Ref. [49]. The shaft mechanical torque was measured through a precision torque meter ($Q_{measured}$), coupled to the electric motor. Bearing losses (Q_{loss}) were measured and the resulting values were successively added to the measured torque, according to:

$$Q_{aero} = Q_{measured} + Q_{loss} \tag{4}$$

The rotational speed (Ω_m) and the rotor phase (azimuthal position of the reference blade) were provided by a 13 bit encoder, and the resulting power was computed as:

$$P_{aero} = \frac{Q_{aero}\Omega_m 2\pi}{60} \tag{5}$$

4. Results and discussion

4.1. Raw data, power and thrust curves

Prior to discuss the results, the most relevant outcomes of the mechanical measurements are first provided. Tables 5–8 (in Appendix I) summarize the measured raw data for the two tested (upright and tilted) operating conditions at 200 *rpm* and 300 *rpm*: freestream wind velocity V_∞ at the test section inlet, ambient temperature Θ and corresponding air density ρ, nominal Ω_n and measured Ω_m rotor angular speeds, aerodynamic torque Q_{aero} and thrusts T in X and Y directions are here presented alongside their uncertainties. It is to be noted that the strain-gauge bridge measures thrust components perpendicular to the rotor axis (see Fig. 3); as a result, the T_X data are referred to the intrinsic coordinate system of the rotor and, hence, are directed in the streamwise direction only when the rotor is in upright configuration. Furthermore, for tilted tests the strain gauge offset was recorded with tilted rotor to find the net wind thrust, avoiding the rotor weight bending moment component.

The overall measurement uncertainties u[95%] and the error propagation for derived measurements, appearing in Tables 5–8 in Appendix I, were both computed following the standard ISO ENV 13005 [50]. The reference wind speed and its uncertainty were derived from the wind tunnel managing system before each measurement. In this case, the B-uncertainty resulted the main term and was equal to ± 0.12 m/s. In Appendix II are provided more details about the error analysis.

The maximum Re^+ and minimum Re^- blade Reynolds numbers appearing in the tables are respectively defined as:

$$Re^+ = \frac{(V_\infty + \Omega R_{eq})c}{\nu}$$
$$Re^- = \frac{(V_\infty - \Omega R_{eq})c}{\nu} \tag{6}$$

and are both evaluated considering the equatorial plane, as commonly done for troposkien rotors.

The direct quantitative analysis of the data is illuminating on the impact of tower tilting on turbine operation. Taking as example the measured data at 300 *rmp* and 9.02 m/s, a 8.2% reduction in work extraction is registered between the VAWT in normal operation (upright, the torque reaches 12.29 Nm) and during the tilted one (11.28 Nm). In the same conditions, thrusts remain almost the same, showing variations less than 5% (in upright condition the X-thrust reaches 97.7 N and the Y-thrust −20.5 N, while in tilted condition X-thrust reaches 94.0 N and Y-thrust −21.6 N). Figs. 7–10 show more clearly a comparison between the measured power and thrust curves, for both upright and tilted operating conditions at $\Omega_n = 200$ *rpm* and $\Omega_n = 300$ *rpm*. The figures contain mean values and measurement uncertainties. It is worth noting that the very small uncertainty in wind speed vanishes in this representation.

As can be clearly seen, the measured power at $\Omega_n = 300$ *rpm* is much higher than the one measured at $\Omega_n = 200$ *rpm*, at least for higher freestream wind speeds (roughly over $V_\infty = 7$ *m/s*), thanks to both a more favourable combination of the relative angles of attack and a higher Reynolds number; as expected, the corresponding thrusts are also increased. It is worth observing that the X forces exerted on the rotor appear to be several times larger than the corresponding Y ones. A reduction in power extraction of the tilted arrangement with respect to the upright one is clearly perceived from Figs. 7 and 9, for both tested angular velocities, at least until the peak power curve. On the contrary, vanishing differences can be drawn from the thrust curves (Figs. 8 and 10).

The hereby presented findings show that for troposkien rotor architectures the torque and the thrust variation due to skewed flow operation may be not directly coupled (the torque reduction in oblique flow appears to be much more pronounced than the corresponding thrust variation, see Figs. 7–10). This suggests that the analytical method proposed by Ferreira et al. [51] to predict the aerodynamic efficiency of an H-Darrieus turbine in skewed flows, devised assuming the thrust variation to follow the same tendency as that of the torque, is not extendable to troposkien turbine architectures.

This finding can be explained thinking at the geometrical differences between the straight architecture and the troposkien one: generally speaking, VAWTs can be schematically represented by two rotor parts, one at the windward side and one at the leeward one; the streamtube crossing the rotor interacts twice with the blades, the leeward side being penalized by the wakes and vortices shed by the blades travelling in the windward one. As already observed by Mertens [37], during skewed flow operation of an H-Darrieus, a significant portion of the flow passes only once through the rotor, its extension depending on both the skew angle and the aspect ratio of the rotor (for high skew angles and low aspect ratios, almost the whole rotor operates as two single rotor portions, thus increasing the effective swept area and, therefore, the aerodynamic power). Conversely, due to the specific geometry of the troposkien rotor (roughly comparable to a sphere, as can be easily drawn from Fig. 11), the 'clean' interaction region observed by Mertens for skewed H-Darrieus is not actually established; in other words, the streamtube crosses twice the rotor also in skewed conditions. Hence, contrarily to the findings of [34,37,40,41,43] for H-shaped VAWTs, in which a performance increase was documented, no extra-power is obtained due to skewed operation.

4.2. Normalized power

To provide more insights on the turbine performance, Figs. 12 and 13 represent the normalized power defined as:

$$C_{P_{aero}} = \frac{P_{aero}}{0.5\rho A_s V_\infty^3} \tag{7}$$

as a function of the equatorial tip speed ratio:

$$TSR_{eq} = \frac{\Omega_m R_{eq}}{V_\infty} \tag{8}$$

for both upright and tilted operating conditions. The TSR_{eq} uncertainty was calculated combining the angular velocity and the wind speed uncertainties [50]. The resulting $u_{TSR_{eq}}$ value is very small and it cannot be perceived in Figs. 12 and 13. As already well known [52–54], a simple comparison between Figs. 12 and 13 can easily highlight how turbine performance is strongly influenced by the local Reynolds number experienced from each blade section. Looking once more at Fig. 12, it can be argued that the negative $C_{P_{aero}}$ band at low TSR_{eq}s could be very small. In other words, extrapolating the proposed measurements to low TSR_{eq} values, the $C_{P_{aero}}$ could be not so small as that obtained during Sandia tests on small VAWTs [18]. Moreover, comparing the $C_{P_{aero}}$-TSR_{eq} curve at 200 rpm (chord Reynolds number of 1.4×10^5) to the one at 300 rpm (chord Reynolds number of 2.5×10^5), it clearly appears that the local (i.e. experienced by each blade section) Reynolds number strongly promotes the energy extraction (see also [52–54]), even at low TSR_{eq}s. The different behaviour of the hereby tested rotor is not to be ascribed to a higher chord Reynolds number (in Ref. [18] the chord Reynolds number ranges from 1×10^5 to 3×10^5), nor to a

different solidity (which, again, is here comparable to the one in Ref. [18]). On the other hand, such difference could be connected with higher stall characteristics of the DU-06-W200 airfoil (characterized by a thickness to chord ratio of 0.18) with respect to the NACA 0012 one (adopted in Ref. [18]). This hypothesis is further confirmed by the findings of [55] where, due to a less sensitivity to blade separation, the computed power curve of a three-bladed NACA 0021 rotor shifted towards lower TSR values with respect to a three-bladed NACA 0012 rotor. As already observed by Ref. [7] in the case of HAWTs, the application of the momentum theory to an actuator disc representing a tilted VAWT is critical, the blade circulation varying with its azimuthal, vertical and streamwise position. Nonetheless, the present findings are consistent with the simple model proposed by Scheurich and Brown [43] for evaluating the performance of a VAWT in oblique flow (based on the swept-wing theory, see Ref. [56,57]). According to such theory, the component of wind speed parallel to the shaft has no effect on rotor aerodynamics, thus determining a reduction of the effective unperturbed velocity perceived by the turbine, which can be simply expressed as:

$$V_{\infty,eff} = V_{\infty}\cos\gamma \tag{9}$$

and a consequent increase of the effective tip speed ratio, in formula:

$$TSR_{eq,eff} = \frac{TSR_{eq}}{\cos\gamma}. \tag{10}$$

Assuming that the tilting does not have any impact on the rotor aerodynamics, and the upstream velocity reduction is the unique effect, the resulting power coefficient can be simply expressed as:

$$C_{P\ aero}(TSR_{eq},\gamma) = C_{P\ aero}\left(TSR_{eq,eff},0\right)\ cos^3\gamma \tag{11}$$

As can be inferred from Figs. 12 and 13, the overall aerodynamic performance of the rotor operating in skewed flow is lowered by the combined effects of reduced effective unperturbed velocity and increased effective tip speed ratio. Nevertheless, if the reduction dependent on $\cos\gamma$ - eqn. (9) - always decreases the aerodynamic efficiency over the whole range of operating conditions, the higher effective tip speed ratio - eqn. (10) - could also increase the rotor performance (depending on the sensitivity of $C_{P\,aero}$ on TSR_{eq}).

Interestingly, eqn. (11) predicts the decay of rotor performance due to tilting in relatively good approximation, as the theoretical results lie within the band of uncertainty of tilted rotor measurements for most of the operating range. This is probably dependent on the troposkien architecture that, as discussed in the previous section, minimizes the sensitivity of rotor aerodynamics on skew; in such a configuration, it is reasonable that the main impact of tilting is on the effective incoming velocity; for these same reasons, it is expected that such a result is not extendable to straight VAWTs.

4.3. Rotor wake measurements

To provide a quantitative description of the wake, Fig. 14 shows the distribution of the time-mean velocity magnitude (averaged over several rotor revolutions) on a vertical plane located 1.5 diameters downstream of the turbine axis. Starting from the peak power curve described in the previous section, wake measurements are hereby proposed for the upright rotor arrangement at the angular velocity of $\Omega_n = 300\ rpm$ (corresponding to an unperturbed wind speed of 9.0 m/s), as well as for the tilted configuration at the same operating conditions.

Thanks to the flow symmetry with respect to the equatorial plane, measurements on the upright configuration are performed only for the lower half of the rotor (up to $z/H = 0.5$); for the tilted arrangement case, where vertical symmetry does not hold, rotor height was investigated from Ref. $z/H = 0.5$ up to $z/H = 0.6$ (namely, the maximum extension available of the vertical traversing).

The wakes roughly resemble the swept area of the troposkien rotor, showing a dramatic narrowing towards the hub, where it merges with the wake of the shaft. The wake also exhibits a relevant horizontal asymmetry, resulting more extended towards negative Y, where higher velocity defects are also found. As observed by Ferreira et al. [40] and, more recently, by Dossena et al. [48], this asymmetry in induced velocity distribution depends on the different relative wind speed that establishes on the blade profiles when they travel on the two sides of the machine. During a full revolution, the interaction of one blade with the wind can be divided into a 'downwind' phase ($0 < y/R_{eq} < 0.5$) and an 'upwind'

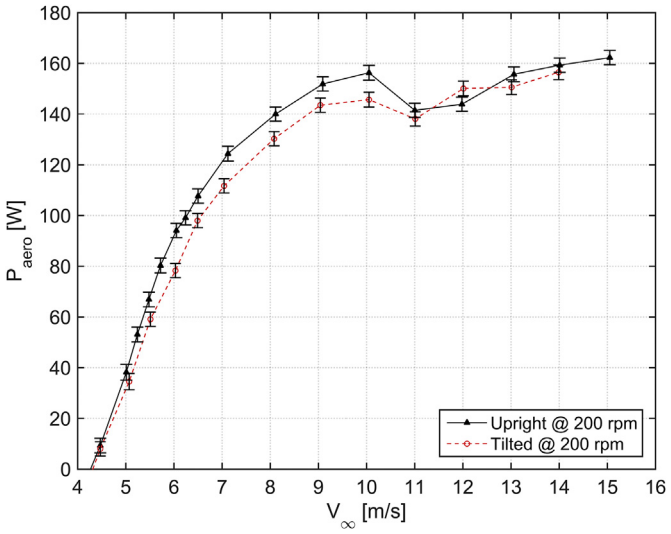

Fig. 7. Comparison between power curves for the two analysed operating conditions at $\Omega_n = 200\ rpm$.

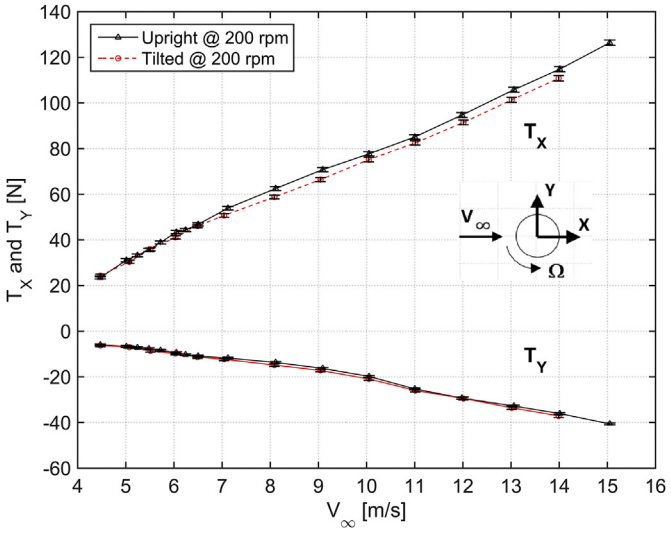

Fig. 8. Comparison between thrusts for the two analysed operating conditions at $\Omega_n = 200\ rpm$.

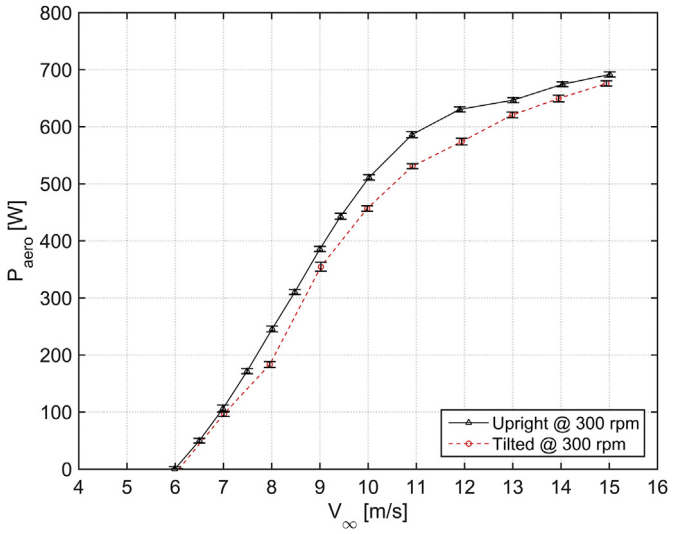

Fig. 9. Comparison between power curves for the two analysed operating conditions at $\Omega_n = 300\,rpm$.

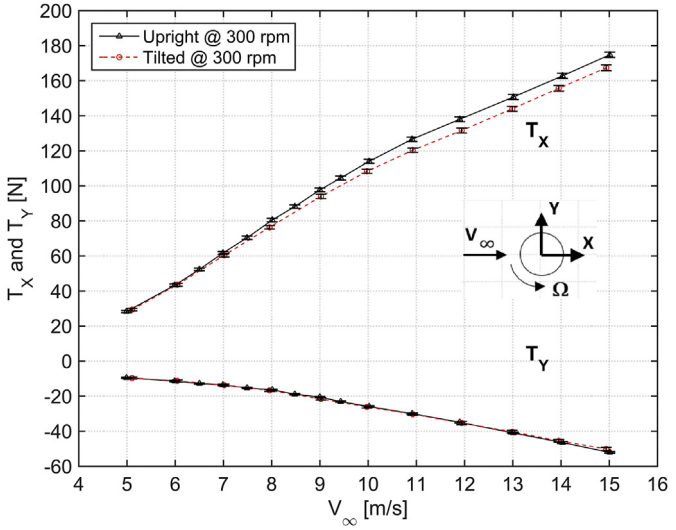

Fig. 10. Comparison between thrusts for the two analysed operating conditions at $\Omega_n = 300\,rpm$.

one ($-0.5<y/R_{eq}<0$): in the upwind phase the blades travel against the wind speed, resulting in a more favourable and less fluctuating blade incidence with respect to the one established during the downwind phase. From this perspective, the larger wake recorded for negative y/R_{eq} can be explained as a result of the more effective work extraction process occurring in the upwind phase.

The general shape of the wake is conserved when the rotor is tilted; however, the lower aerodynamic efficiency of the tilted rotor is readily perceived comparing Fig. 14-top and Fig. 14-bottom: the higher power extraction of the upright arrangement clearly results in a larger momentum loss and, consequently, a lower velocity in the wake. Moreover, the wake slightly changes its shape close to the hub, where it further enlarges towards negative y/R_{eq} with respect to its upfront counterpart. These results indicate that the tilting does have an impact on the rotor aerodynamics, mostly confined in the hub region of the machine as found for H-shaped Darrieus in skewed flows; however, since in troposkien rotors most of the work is exchanged in the midspan region, the quantitative contribution of these effects on the overall power is limited. This further justifies the assumption that, for troposkien VAWTs, the most relevant effect of tilting is the change in effective upstream wind speed and not the alteration in the rotor aerodynamics.

To highlight the turbulence properties of the wake, Fig. 15 reports the distribution of turbulence intensity (based on the streamwise turbulent velocity component) on the measurement traverses downstream of the rotor. Considering the very low turbulence intensity in the turbine incoming flow (below 1%), the plots here reported can be regarded as the turbulence generated by the viscous effects activated on the turbine profiles and on the rotor shaft, as well as the one arising from the mixing process occurring in the near wake.

To determine the turbulence intensity, the phase-resolved velocity component (i.e., the one connected to the blade passing frequency) was first eliminated from the instantaneous velocity signal; the resulting 'unresolved' unsteady fluctuation can be interpreted as the turbulent velocity component in streamwise direction, whose root mean square σ_V is here used to quantify the turbulence intensity as follows:

$$I_{TU} = \frac{\sigma_V}{V_\infty} \tag{12}$$

The turbulence intensity fields allow to properly identify the margins of the wake, as an increase of turbulence is registered in the whole wake region with respect to that of the external flow.

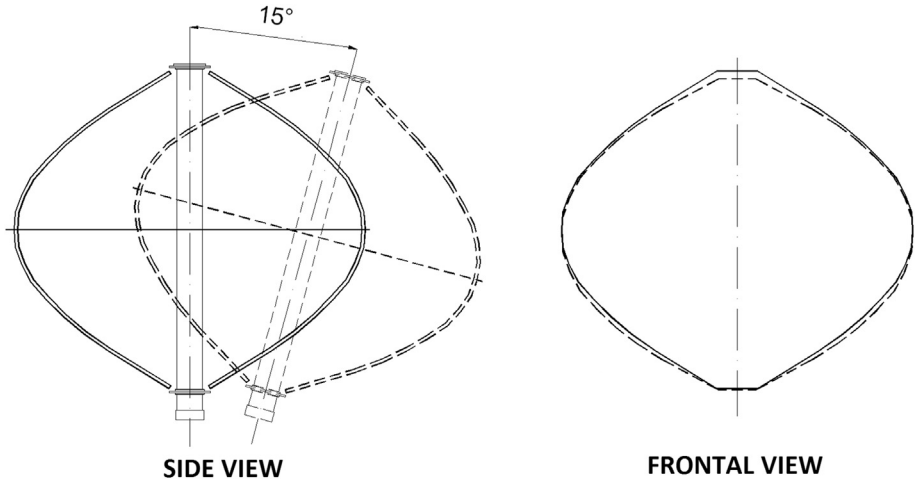

Fig. 11. Visual comparison between the swept area of the upright rotor (continuous line) and the vertical projection of the swept area of the tilted one (dashed line).

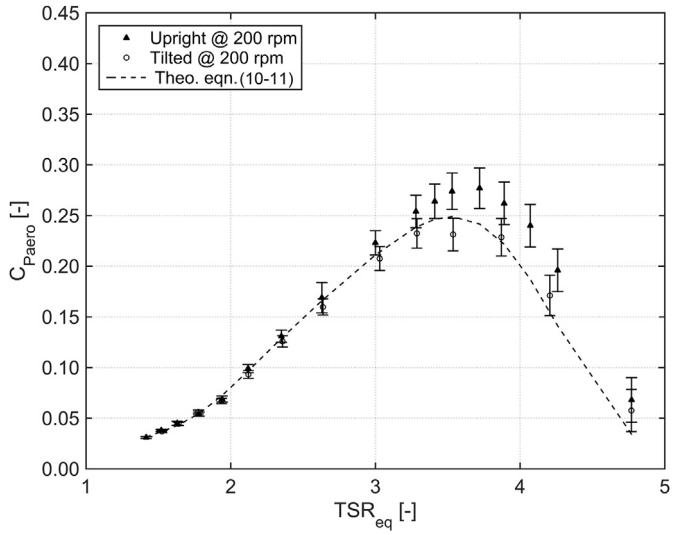

Fig. 12. Rotor power coefficient, eqn. (7), as a function of the equivalent tip speed ratio for the two analysed operating conditions at $\Omega_n = 200\,rpm$; the power coefficient derived from the simple theory by Ref. [43], computed according eqns. (10) and (11), is also shown.

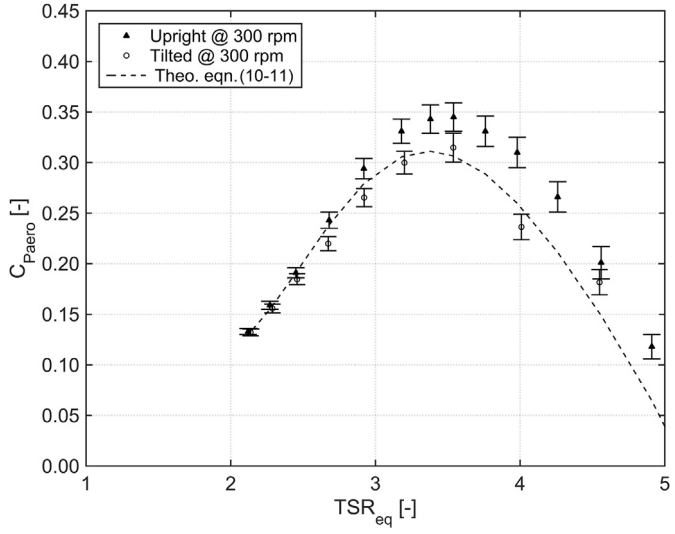

Fig. 13. Rotor power coefficient, eqn. (7), as a function of the equivalent tip speed ratio for the two analysed operating conditions at $\Omega_n = 300\,rpm$; the power coefficient derived from the simple theory by Ref. [43], computed according eqns. (10) and (11), is also shown (the same scale of the $\Omega_n = 200\,rpm$ case is adopted).

However, large disuniformities are found within the wake: higher turbulence is detected on the wake edges, where the onset of shear layers between the wake and the outer flow promotes turbulent mixing, and close to the wake centreline, where the viscous wake shed by the shaft reaches the measurement traverse. In-between these high-turbulence regions, and far from the rotor hub, the turbulence intensity reduces significantly on both the wake sides, approaching the values of the external undisturbed flow.

The most striking gradients are found moving towards the rotor hub, where the lateral shear layer of the wake merges with the viscous wake of the shaft, resulting in the highest peaks of turbulence intensity. The hub wake exhibits a highly non-symmetrical character, much higher turbulence being generated in the 'downwind' side of the wake. This is probably due to the very low tip speed ratio locally established in the hub of the troposkien turbine: in this part of the machine, and in particular during the downwind part of the revolution, the blades experience the largest incidence oscillations, being prone to dynamic stall which triggers a severe turbulence production in the wake. The distributions reported in Fig. 15 indicate that, for the rotor operating in upright conditions, highly turbulent phenomena characterize the downwind side of the wake only below 25% of the rotor span, while very low turbulence is found in the midspan region. When the rotor is tilted, a similar pattern is observed even though the high turbulence region in the downwind side of the wake is more elongated spanwise and nearly reaches midspan; the tilting does alter the incidence on the blades (due to the reduction of active wind speed related to $\cos\gamma$), and its impact is likely to be more pronounced in the downwind part of the revolution when the profiles are prone to stall. This is a further indication that, for troposkien turbine configurations, the tilting has a negative impact on aerodynamic performance.

5. Conclusions

The first experimental investigation of a Darrieus VAWT operating in skewed flow was presented. The effect of tower tilting on rotor aerodynamics and performance was investigated by means of a comprehensive measurement campaign, with the aim of reproducing the operation in skewed flow of a floating VAWT at its maximum allowable pitch angle (15°). A substantial lack of experimental data was recognized related to offshore semi-submersible installations; a comparison with measurements on H-VAWTs operating in skewed flow was nonetheless achieved, by resorting to previous experimental campaigns aiming at the investigation of wind energy conversion systems placed on top of high-rise buildings.

Specific care was taken in the description of the experimental set-up and of the measured data, providing a full set of information about the modelling of both rotor and test arrangement, as well as the boundary conditions to be imposed for reproducing the presented results, in view of future computational investigations. To also provide a quantitative description of the wake, both the velocity and turbulence intensity distributions measured on a vertical plane located 1.5 diameters downstream of the rotor shaft were reported.

Despite the limitations of the scaled rotor model (primarily the inability to match the Reynolds numbers of the full-scale machine), the results here presented clearly show that hypotheses drawn about skewed flow operation from available data on H-VAWTs cannot be extended to troposkien turbine configurations.

As the geometry of the troposkien rotor is roughly comparable to a sphere, a very small variation of the energy extraction area was registered as a consequence of the shaft inclination. Hence, contrarily to what found by authors focused on H-VAWTs, no increment of power output was obtained when passing from upright to tilted operation. In fact, the present findings are consistent with a very simple model, based on the swept-wing theory, that evaluates the performance of a VAWT in oblique flow by assuming that the component of wind speed parallel to the shaft has no effect on rotor aerodynamics. Accordingly, the tilting produces a reduction of the effective unperturbed velocity perceived by the turbine as well as an increase of its effective tip speed ratio and a reduction of power coefficient. Moreover, in contrast to other authors' findings, the torque reduction in oblique flow appears to be much more pronounced than the corresponding thrust variation.

The flow configuration in the wake appears to be consistent with these findings. The midspan region of the wake is weakly affected by the tilting, even though a reduction of induced velocity is observed when the rotor is inclined, in line with the model prediction. The impact of the shaft inclination is more relevant in

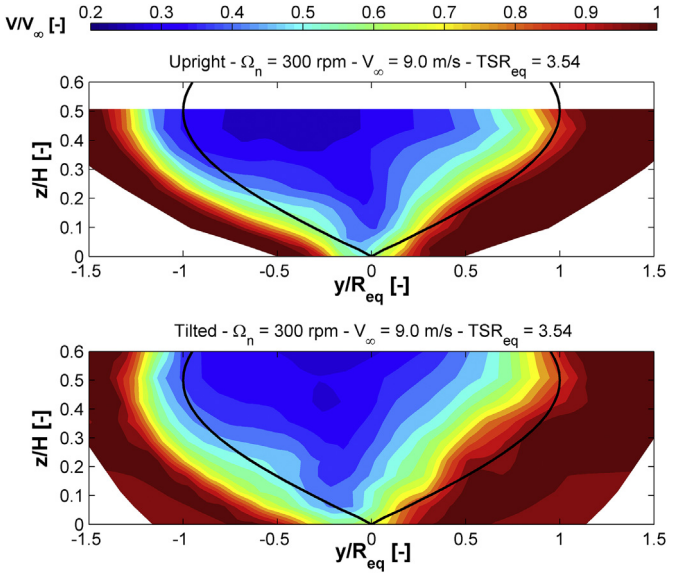

Fig. 14. Time-mean velocity magnitude (normalized with the unperturbed wind speed at the test section entrance) on a vertical plane located 1.5 diameters downstream of the test section (observed looking downstream through the rotor), for different operating conditions (the projection of rotor swept area is also represented by means of continuous black lines).

the hub region of the wake, as occurs for H-VAWTs; however, the highly tapered shape of the troposkien rotor does not allow to exploit the potential of the 'clean' part of the flow in this region, which provides a modest contribution to the power exchange; conversely, the aerodynamics of this region seems to be further penalized by the inclination, as marked by a net increase of turbulence intensity.

Beside these initial findings, focused on the time-mean characterization of the VAWT aerodynamics, the here presented test

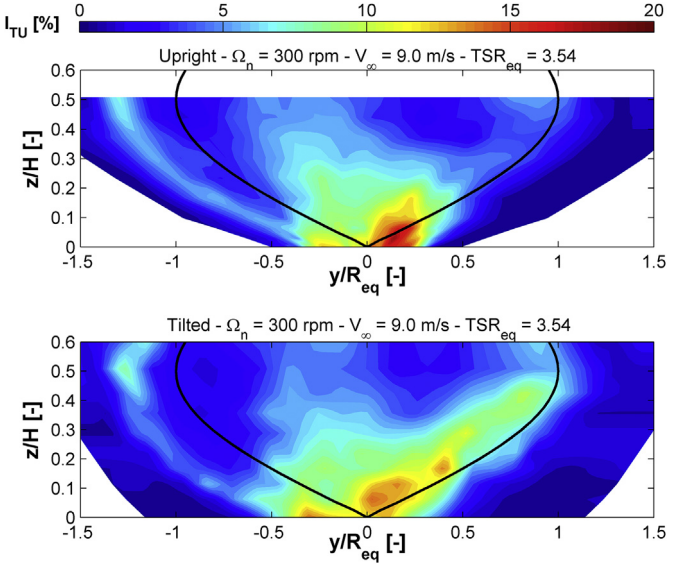

Fig. 15. Time-mean turbulence contours on a vertical plane located 1.5 diameters downstream of the test section (observed looking downstream through the rotor), for different operating conditions (the projection of rotor swept area is also represented by means of continuous black lines).

arrangement has the potential for deeper investigations on the unsteady evolution of both performance and loads during rotor revolution, as well as the characterization of the wake meandering downstream of the rotor test section. Plans are undergoing to further explore the three dimensional features of both upright and tilted rotor wakes, as well as their time-periodic evolution, by resorting to an integrated experimental and CFD campaign, with the aim of further understanding the aerodynamics of skewed VAWT operation.

Acknowledgements

The present work is a result of the contributions from the DeepWind project, supported by the European Commission, Grant 256769 FP7 Energy 2010 - Future emerging technologies, and by the DeepWind beneficiaries: DTU(DK), AAU(DK), TUDELFT(NL), TUTRENTO(I), DHI(DK), SINTEF(N), MARINTEK(N), MARIN(NL), NREL(USA), STATOIL(N), VESTAS(DK) and NENUPHAR(F).

List of main symbols

Latin

A_s	rotor swept area [m^2]
$A_{s,tilted}$	tilted rotor swept area [m^2]
B	rotor blade number [−]
c	airfoil chord length [m]
C_X	rotor X thrust coefficient [−]
C_Y	rotor Y thrust coefficient [−]
$C_{P,aero}$	aerodynamic power coefficient [−]
$C_{P,eff}$	effective aerodynamic power coefficient [−]
C_Q	aerodynamic torque coefficient [−]
d	distance between strain-gauges and rotor mid span [m]
H	rotor height [m]
H_{wt}	wind tunnel height [m]
I_{TU}	turbulence intensity [%]
I_z	rotor moment of inertia around shaft [kg m^2]
L	blade length [m]
M	rotor weight [kg]
Q_{aero}	aerodynamic torque [Nm]
P_{aero}	aerodynamic power [W]
Re^+	maximum blade Reynolds number $= (V_\infty + \Omega R_{eq})\, c/\nu$ [−]
Re^-	minimum blade Reynolds number $= (V_\infty - \Omega R_{eq})\, c/\nu$ [−]
R_{eq}	equatorial rotor radius [m]
t	airfoil thickness [m]
$TSR_{eq,eff}$	effective tip speed ratio $= TSR_{eq}/\cos\gamma$ [−]
TSR_{eq}	equatorial tip speed ratio $= \Omega_n R_{eq}/V_\infty$ [−]
TSR_{max}	equatorial tip speed ratio of maximum power coefficient [−]
T_X	rotor X thrust [N]
T_Y	rotor Y thrust [N]
u_{Qaero}	aerodynamic torque uncertainty [Nm]
u_{T_X}	X thrust uncertainty [N]
u_{T_Y}	Y thrust uncertainty [N]
u_{V_∞}	velocity uncertainty [m/s]
u_Θ	temperature uncertainty [°C]
u_ρ	density uncertainty [kg/m^3]
u_{Ω_m}	angular velocity uncertainty [rpm]
u_{TSR}	tip speed ratio uncertainty [−]
V	local streamwise velocity measured on the vertical plane located 1.5 diameters downstream of the test section [m/s]
V_∞	freestream speed [m/s]
$V_{\infty,eff}$	effective freestream speed $= V_\infty \cos\gamma$ [m/s]
W_{wt}	wind tunnel width [m]

z local rotor height [m]
z_0 ground roughness length [m]

Greek
β rotor diameter/height ratio = H/2 R_{eq} [−]
γ tilt angle [°]
ε 3D geometric blockage [%]
Θ freestream temperature [°C]
ν freestream kinematic viscosity [m^2/s]
ρ freestream density [kg/m^3]
σ rotor solidity = BLc/A_s [−]
σ_V standard deviation of the local streamwise velocity [m/s]
Ω_m measured rotor angular velocity [rpm]
Ω_n nominal rotor angular velocity [rpm]

Coordinate system
x, y, z coordinates
X, Y, Z turbine axis system
X_{WP}, Y_{WP}, Z_{WP} wake measurement axis system

Acronyms
BAWT building augmented wind turbine
BEM blade element momentum
CFD computational fluid dynamics
DoE department of energy
HAWT horizontal axis wind turbine
H-Darrieus straight bladed Darrieus wind turbine
LCoE levelized cost of energy
PIV particle image velocimetry
SGAP strain gauges application point
VAWT vertical axis wind turbine
VTM vorticity transport model
WECS wind energy conversion system

Appendix I. Tabular experimental data

This section presents the results of the tests carried out on the 3-bladed Darrieus wind turbine in the open chamber wind tunnel. Measurements at rotor angular speed of 200 rpm (approximately corresponding to a Reynolds number of 1.4×10^5) are collected in Table 5 (rotor in upright position) and Table 6 (in tilted position), while the ones taken at rotor angular speed of 300 rpm (approximately corresponding to a Reynolds number of 2.1×10^5) are collected in Table 7 (rotor in upright position) and Table 8 (in tilted position). The meaning of the nomenclature here adopted is fully detailed in the paper and in the list of symbols.

Table 5
Upright rotor at Ω_n = 200 rpm.

V_∞ [m/s]	u_{V_∞}[95%] [m/s]	Θ [°C]	u_Θ[95%] [°C]	ρ [kg/m^3]	u_ρ[95%] [kg/m^3]	Ω_m [rpm]	u_{Ω_m}[95%] [rpm]	Q_{aero} [Nm]	$u_{Q_{aero}}$[95%] [Nm]	T_X [N]	u_{T_X}[95%] [N]	T_Y [N]	u_{T_Y}[95%] [N]	Re^+ [−]	Re^- [−]
4.00	0.12	20.7	0.1	1.179	0.002	200.7	0.2	−0.58	0.13	19.2	0.6	−5.4	0.5	1.6E + 05	1.1E + 05
4.47	0.12	21.6	0.1	1.174	0.002	200.7	0.1	0.44	0.14	23.5	0.6	−6.0	0.5	1.7E + 05	1.1E + 05
5.01	0.12	20.6	0.1	1.179	0.002	200.7	0.7	1.82	0.15	31.0	0.7	−6.7	0.5	1.7E + 05	1.1E + 05
5.24	0.12	21.4	0.1	1.173	0.002	200.5	0.1	2.53	0.14	33.1	0.6	−7.2	0.5	1.7E + 05	1.0E + 05
5.48	0.12	20.8	0.1	1.176	0.002	200.7	0.2	3.18	0.14	35.5	0.7	−7.7	0.5	1.7E + 05	1.0E + 05
5.72	0.12	21.2	0.1	1.174	0.002	200.5	0.1	3.82	0.14	38.8	0.7	−8.4	0.5	1.7E + 05	1.0E + 05
6.05	0.12	20.6	0.1	1.179	0.002	200.7	0.1	4.48	0.13	43.3	0.7	−9.4	0.5	1.8E + 05	9.9E + 04
6.24	0.12	21.2	0.1	1.174	0.002	200.5	0.3	4.72	0.13	44.2	0.7	−10.3	0.5	1.8E + 05	9.7E + 04
6.50	0.12	20.8	0.1	1.176	0.002	200.7	0.1	5.12	0.13	46.6	0.7	−10.9	0.5	1.8E + 05	9.6E + 04
7.12	0.12	20.8	0.1	1.178	0.002	200.7	0.1	5.92	0.14	53.7	0.8	−11.7	0.5	1.8E + 05	9.2E + 04
8.11	0.12	20.8	0.1	1.178	0.002	200.7	0.2	6.66	0.13	62.3	0.9	−13.6	0.5	1.9E + 05	8.5E + 04
9.09	0.12	20.9	0.1	1.177	0.002	200.7	0.1	7.23	0.13	70.6	0.9	−16.2	0.6	2.0E + 05	7.9E + 04
10.05	0.12	21.2	0.1	1.176	0.002	200.7	0.2	7.44	0.14	77.5	0.9	−19.7	0.6	2.0E + 05	7.3E + 04
11.00	0.12	21.0	0.1	1.175	0.002	200.7	0.1	6.73	0.13	84.9	1.0	−25.3	0.6	2.1E + 05	6.7E + 04
11.98	0.12	21.0	0.1	1.175	0.002	200.7	0.2	6.85	0.13	94.4	1.0	−29.2	0.7	2.1E + 05	6.0E + 04
13.06	0.12	21.2	0.1	1.175	0.002	200.7	0.2	7.41	0.14	105.5	1.1	−32.7	0.7	2.2E + 05	5.3E + 04
14.01	0.12	21.2	0.1	1.174	0.002	200.5	0.1	7.59	0.13	114.5	1.1	−36.0	0.7	2.3E + 05	4.7E + 04
15.05	0.12	21.1	0.1	1.168	0.002	200.4	0.0	7.73	0.13	126.1	1.2	−40.5	0.7	2.3E + 05	4.0E + 04

Table 6
Tilted rotor at Ω_n = 200 rpm.

V_∞ [m/s]	u_{V_∞}[95%] [m/s]	Θ [°C]	u_Θ[95%] [°C]	ρ [kg/m^3]	u_ρ[95%] [kg/m^3]	Ω_m [rpm]	u_{Ω_m}[95%] [rpm]	Q_{aero} [Nm]	$u_{Q_{aero}}$[95%] [Nm]	T_X [N]	u_{T_X}[95%] [N]	T_Y [N]	u_{T_Y}[95%] [N]	Re^+ [−]	Re^- [−]
4.47	0.12	20.9	0.1	1.175	0.002	200.7	0.2	0.38	0.13	24.4	0.6	−6.3	0.5	1.7E + 05	1.1E + 05
5.07	0.12	21.1	0.1	1.173	0.002	200.7	0.1	1.64	0.15	30.4	0.7	−7.0	0.5	1.7E + 05	1.0E + 05
5.51	0.12	20.7	0.1	1.175	0.002	200.6	0.1	2.81	0.13	35.8	0.7	−8.7	0.5	1.7E + 05	1.0E + 05
6.03	0.12	21.1	0.1	1.173	0.002	200.7	0.2	3.72	0.13	41.1	0.7	−9.8	0.5	1.8E + 05	9.9E + 04
6.49	0.12	20.7	0.1	1.175	0.002	200.6	0.1	4.67	0.13	46.1	0.7	−11.4	0.5	1.8E + 05	9.6E + 04
7.04	0.12	21.1	0.1	1.173	0.002	200.7	0.1	5.31	0.13	50.7	0.8	−12.4	0.5	1.8E + 05	9.2E + 04
8.08	0.12	21.2	0.1	1.173	0.002	200.6	0.1	6.20	0.13	58.8	0.8	−14.8	0.6	1.9E + 05	8.5E + 04
9.04	0.12	21.2	0.1	1.173	0.002	200.6	0.3	6.83	0.13	66.4	0.9	−17.2	0.6	2.0E + 05	7.9E + 04
10.05	0.12	21.2	0.1	1.173	0.002	200.6	0.2	6.94	0.14	75.2	1.0	−20.9	0.6	2.0E + 05	7.3E + 04
11.01	0.12	21.3	0.1	1.173	0.002	200.6	0.1	6.57	0.13	82.5	1.0	−26.0	0.6	2.1E + 05	6.7E + 04
12.01	0.12	21.3	0.1	1.173	0.002	200.6	0.2	7.14	0.14	91.5	1.0	−29.5	0.7	2.2E + 05	6.0E + 04
13.01	0.12	21.3	0.1	1.173	0.002	200.6	0.3	7.17	0.14	101.4	1.1	−33.6	0.7	2.2E + 05	5.4E + 04
13.99	0.12	21.3	0.1	1.173	0.002	200.6	0.1	7.45	0.14	110.8	1.2	−37.1	0.7	2.3E + 05	4.7E + 04

Table 7
Upright rotor at $\Omega_n = 300$ rpm.

V_∞ [m/s]	u_{V_∞} [95%] [m/s]	Θ [°C]	u_Θ[95%] [°C]	ρ [kg/m^3]	u_ρ[95%] [kg/m^3]	Ω_m [rpm]	u_{Ω_m} [95%] [rpm]	Q_{aero} [Nm]	$u_{Q_{aero}}$ [95%] [Nm]	T_X [N]	u_{T_X} [95%] [N]	T_Y [N]	u_{T_Y} [95%] [N]	Re^+ [−]	Re^- [−]
3.97	0.12	21.2	0.1	1.174	0.002	305.4	0.1	−3.62	0.13	18.5	0.6	−8.2	0.4	2.4E + 05	1.8E + 05
4.99	0.12	21.0	0.1	1.175	0.002	300.1	0.2	−2.33	0.14	28.3	0.6	−9.5	0.4	2.4E + 05	1.7E + 05
5.99	0.12	21.0	0.1	1.175	0.002	300.1	0.1	0.00	0.13	43.3	0.7	−11.4	0.4	2.4E + 05	1.7E + 05
6.50	0.12	21.1	0.1	1.168	0.002	300.1	0.1	1.59	0.13	52.3	0.8	−12.8	0.4	2.5E + 05	1.6E + 05
6.99	0.12	21.0	0.1	1.174	0.002	300.1	0.2	3.37	0.20	61.7	0.8	−13.6	0.4	2.5E + 05	1.6E + 05
7.49	0.12	21.1	0.1	1.168	0.002	300.1	0.1	5.46	0.15	70.4	0.9	−15.3	0.4	2.5E + 05	1.6E + 05
8.01	0.12	21.0	0.1	1.170	0.002	300.0	0.1	7.82	0.16	80.5	1.0	−16.4	0.4	2.6E + 05	1.5E + 05
8.48	0.12	21.0	0.1	1.169	0.002	300.1	0.1	9.88	0.14	88.2	1.0	−18.9	0.4	2.6E + 05	1.5E + 05
9.00	0.12	20.9	0.1	1.170	0.002	300.0	0.1	12.29	0.14	97.7	1.1	−20.5	0.4	2.6E + 05	1.5E + 05
9.43	0.12	21.0	0.1	1.169	0.002	300.1	0.1	14.10	0.17	104.5	1.2	−23.1	0.4	2.7E + 05	1.4E + 05
10.02	0.12	20.8	0.1	1.170	0.002	300.0	0.1	16.28	0.15	114.0	1.2	−25.9	0.4	2.7E + 05	1.4E + 05
10.91	0.12	20.9	0.1	1.169	0.002	300.0	0.1	18.66	0.17	126.6	1.2	−30.0	0.4	2.8E + 05	1.4E + 05
11.90	0.12	20.9	0.1	1.169	0.002	300.0	0.1	20.07	0.14	138.0	1.3	−34.9	0.4	2.8E + 05	1.3E + 05
13.01	0.12	21.0	0.1	1.169	0.002	300.0	0.2	20.59	0.14	150.7	1.5	−41.0	0.4	2.9E + 05	1.2E + 05
14.03	0.12	21.1	0.1	1.168	0.002	300.0	0.1	21.47	0.13	162.8	1.5	−46.5	0.5	3.0E + 05	1.2E + 05
15.01	0.12	21.1	0.1	1.168	0.002	300.0	0.1	22.02	0.14	174.8	1.5	−52.1	0.4	3.0E + 05	1.1E + 05

Table 8
Tilted rotor at $\Omega_n = 300$ rpm.

V_∞ [m/s]	u_{V_∞} [95%] [m/s]	Θ [°C]	u_Θ[95%] [°C]	ρ [kg/m^3]	u_ρ[95%] [kg/m^3]	Ω_m [rpm]	u_{Ω_m} [95%] [rpm]	Q_{aero} [Nm]	$u_{Q_{aero}}$ [95%] [Nm]	T_X [N]	u_{T_X} [95%] [N]	T_Y [N]	u_{T_Y} [95%] [N]	Re^+ [−]	Re^- [−]
5.10	0.12	21.2	0.1	1.173	0.002	300.3	0.1	−2.21	0.13	29.4	0.7	−9.6	0.6	2.4E + 05	1.7E + 05
6.04	0.12	21.2	0.1	1.173	0.002	300.3	0.3	−0.11	0.15	43.5	0.8	−11.3	0.6	2.4E + 05	1.7E + 05
7.01	0.12	21.3	0.1	1.172	0.002	300.2	0.1	3.08	0.14	60.4	1.0	−13.7	0.6	2.5E + 05	1.6E + 05
7.96	0.12	21.3	0.1	1.172	0.002	300.1	0.1	5.84	0.16	76.4	1.0	−16.7	0.6	2.6E + 05	1.5E + 05
9.02	0.12	21.2	0.1	1.167	0.002	300.3	0.1	11.28	0.25	94.0	1.2	−21.6	0.6	2.6E + 05	1.5E + 05
9.98	0.12	21.3	0.1	1.167	0.002	300.3	0.3	14.52	0.15	108.3	1.2	−26.1	0.7	2.7E + 05	1.4E + 05
10.92	0.12	21.3	0.1	1.167	0.002	300.3	0.1	16.88	0.13	120.3	1.2	−30.2	0.7	2.8E + 05	1.4E + 05
11.94	0.12	21.3	0.1	1.167	0.002	300.4	0.4	18.25	0.18	131.6	1.4	−35.4	0.9	2.8E + 05	1.3E + 05
12.99	0.12	21.4	0.1	1.167	0.002	300.4	0.0	19.73	0.16	144.0	1.4	−40.3	0.8	2.9E + 05	1.2E + 05
13.95	0.12	21.4	0.1	1.167	0.002	300.4	0.1	20.65	0.18	155.7	1.6	−45.5	0.8	3.0E + 05	1.2E + 05
14.94	0.12	21.4	0.1	1.167	0.002	300.4	0.3	21.49	0.14	167.4	1.7	−50.1	0.9	3.0E + 05	1.1E + 05

Appendix II. Uncertainty analysis

A measurement uncertainty analysis was conducted by resorting to the standard ISO ENV 13005 *Guide to the expression of Uncertainty in Measurement* [50]. The methodology is deeply explained in the adopted standard and is not here reported again for brevity's sake: just a few words of explanation are here proposed in order to allow a better comprehension in the Reader.

All the variables measured during the experimental tests (collected in Table 4) were monitored focusing to the steady characterization of the DeepWind demonstrator. Most of them are affected by a large dispersion of the measured values during each rotor revolution, because of the peculiar VAWT aerodynamic behaviour. In order to evaluate the magnitude of the uncertainty, the data reduction process was performed as follows:

- for each test (characterized by a rotor angular speed and a wind tunnel speed), the measured time series were divided into 1-revolution bins and all the bin mean values were computed. Starting from these bin mean values, the final averaged measured data were then computed, and the results were reported in Tables 5–8;
- in the same manner, the standard deviation and the type A measurement uncertainty were determined. In this way, the standard deviation contains information about the measurement unsteadiness (uncertainty of repeatability) and not about the turbine aerodynamic unsteadiness. The computed standard uncertainty resulted very small, thanks both to the high-performing wind tunnel and VAWT controller devices;
- in order to perform a more conservative error evaluation, the type B uncertainties were also calculated, sensors accuracy were taken by the manufacturer data sheets (as assessed in the ISO ENV 13005 [50]) and assuming a data rectangular distribution;
- the expected uncertainty $u_{[95\%]}$, having a 95% level of confidence, was then determined and the results were collected in Tables 5–8;
- finally, according to Chapter 5 of [50], the combined standard uncertainty of the derived measurements (as P, T, TSR_{eq} and $C_{P_{aero}}$ values) was determined. Once again, the resulting expected uncertainty $u_{[95\%]}$ was evaluated, and a graphical representation of the results was reported in Figs. 7, 9, 12 and 13.

References

[1] Carlin P, Laxson A, Muljadi E. The history and state of the art of variable-speed wind turbine technology. Wind Energy 2003;6(2):129–59.
[2] Hunt V. Windpower: a handbook on wind energy conversion systems. Van Nostrand Reinhold Co; 1981. ISBN 978–0442273897.
[3] Hofmann M, Sperstad I. Will 10 MW wind turbines bring down the operation and maintenance cost of offshore wind farms? Energy Procedia 2014;53:231–8.
[4] Polinder H, D B, Rooij RV, McDonald A, Mueller M. 10 MW wind turbine direct-drive generator design with pitch or active speed stall control. In: International electric machines and drives conference, antalya (TR), may 3-5; 2007.
[5] Xudong W, Shen W, Zhu W, Sorensen J, Jin C. Shape optimization of wind turbine blades. Wind Energy 2009;12(8):781–803.
[6] S. Mortazavi, M. Soltani, H. Motieyan, A pareto optimal multi-objective optimization for a horizontal axis wind turbine blade airfoil sections utilizing

exergy analysis and neural networks, J Wind Eng Industrial Aerodynamics 136 (62–72).
[7] Burton T, Sharpe D, Jenkins N, Bossanyi E. Wind energy handbook. 2nd ed. John Wiley & Sons Ltd; 2011. ISBN 978-0-470-69975-1.
[8] Fingersh L, Hand M, Laxson A. Wind turbine design cost and scaling model. Tech. Rep. NREL/TP-500–40566. U.S. National Renewable Energy Laboratory; Dec. 2007.
[9] Jonkman J. Dynamics modeling and loads analysis of an offshore floating wind turbine. Tech. Rep. NREL/TP-500–41958. U.S. National Renewable Energy Laboratory; Nov. 2007.
[10] Landberg L, Myllerup L, Rathmann O, Petersen E, Jorgensen B, Badger J, et al. Wind resource estimation - an overview. Wind Energy 2003;6(3):261–71.
[11] Hansen M. Aerodynamics of wind turbines. 2nd ed. James & James (Science Publishers) Ltd; 2008. ISBN 978-1-84407-438-9.
[12] Lange B, Hojstrup J. Evaluation of the wind-resource estimation program WAsP for offshore applications. J Wind Eng Industrial Aerodynamics 2001;89(3–4):271–91.
[13] Henderson A, Morgan C, Smith B, Sorensen H, Barthelmie R, Boesmans B. Offshore wind energy in Europe? A review of the state-of-the-art. Wind Energy 2003;6(1):35–52.
[14] Zaaijer M. Review of knowledge development for the design of offshore wind energy technology. Wind Energy 2009;12(5):411–30.
[15] Musial W, Ram B. Large-scale offshore wind power in the united states - assessment of opportunities and barriers. Tech. Rep. NREL/TP-500–40745. U.S. National Renewable Energy Laboratory; Sept. 2010.
[16] Stoddard W. The life and work of bill heronemus. Wind Eng 2002;26(5): 335–41.
[17] Arapogianni A, Genachte A. Deep water - the next step for offshore wind energy. Ewea report. European Wind Energy Association; July 2013.
[18] Blackwell B, Sheldahl R, Feltz L. Wind tunnel performance data for the Darrieus wind turbine with NACA 0012 blades. Tech. Rep. SAND76–0130. Sandia National Laboratories; May 1976.
[19] Sheldahl R, Blackwell B. Free-air performance tests of a 5-metre-diameter Darrieus turbine. Tech. Rep. SAND77–1063. Sandia National Laboratories; Dec. 1977.
[20] Worstell M. Aerodynamic performance of the 17 meter diameter Darrieus wind turbine. Tech. Rep. SAND78–1737. Sandia National Laboratories; Sept. 1978.
[21] Sheldahl R, Klimas P, Feltz L. Aerodynamic performance of a 5-metre-diameter Darrieus turbine with extruded aluminum NACA-0015 blades. Tech. Rep. SAND80–0179. Sandia National Laboratories; Mar. 1980.
[22] Sheldahl R. Comparison of field and wind tunnel darrieus wind turbine data. Tech. Rep. SAND80–2469. Sandia National Laboratories; Jan. 1981.
[23] Worstell M. Aerodynamic performance of the 17 meter diameter Darrieus wind turbine in the three-bladed configuration: an addendum. Tech. Rep. SAND79–1753. Sandia National Laboratories; Aug. 1982.
[24] Shafer D, Strawmyer K, Conley R, Guidinger J, Wilkie D, Zellman T. WindPACT turbine design scaling studies: technical area 4-balance-of-station cost. Tech. Rep. NREL/SR-500–29950. U.S. National Renewable Energy Laboratory; July 2001.
[25] Saur G, Maples B, Meadows B, Hand M, Musial W, Elkinton C, et al. Offshore wind plant balance-of-station cost drivers and sensitives. In: Offshore windpower 2012, Virginia Beach (US); 2012.
[26] Fowler M, Bull D, Goupee A. A comparison of platform options for deep-water floating offshore Vertical Axis Wind Turbines: an initial study. Tech. Rep. SAND2014–16800. Sandia National Laboratories; Aug. 2014.
[27] Vita L. Offshore floating vertical axis wind turbines with rotating platform. Ph.D. thesis. Technical University of Denmark; Aug. 2011.
[28] Berthelsen P, Fylling I, Vita L, Paulsen U. Conceptual design of a floating support structure and mooring system for a Vertical Axis Wind Turbine. In: 1st international conference on ocean, offshore and arctic engineering (OMAE 2012). Rio de Janeiro (BR): ASME; 2012.
[29] Paulsen U, Madsen H, Hattel J, Baran I, Nielsen P. Design optimization of a 5 MW floating offshore Vertical-Axis wind turbine. Energy Procedia 2013;35: 22–32.
[30] Paulsen U, Madsen H, Kragh KA, Nielsen PH, Baran I, Hattel J, et al. Deepwind-from idea to 5 MW concept. Energy Procedia 2014;53:23–33.
[31] Paulsen U, Pedersen T, Madsen H, Enevoldsen K, Nielsen P, Hattel J, et al. DeepWind - an innovative wind turbine concept for offshore. In: Ewea 2011 conference, Brussels (be); 2011.
[32] Henderson A, Witcher D. Floating offshore wind energy - a review of the current status and an assessment of the prospects. Wind Eng 2010;34(1): 1–16.
[33] Paulsen U, Vita L, Madsen H, Hattel J, Ritchie E, Leban K, et al. 1st DeepWind 5 MW baseline design. Energy Procedia 2012;24:27–35.
[34] Wang K, Hansen M, Moan T. Model improvements for evaluating the effect of tower tilting on the aerodynamics of a vertical axis wind turbine. Wind Energy 2015;18:91–110.
[35] Paraschivoiu I. Double-multiple streamtube model for Darrieus in turbines. In: Wind turbine dynamics; 1981.
[36] Paraschivoiu I, Delclaux F. Double multiple streamtube model with recent improvements. J Energy 1983;7:250–5.
[37] Mertens S, van Kuik G, van Bussel G. Performance of an h-darrieus in the skewed flow on a roof. J Sol Energy Eng 2003:433–40.
[38] Mertens S. Wind energy in the built environment - concentrator effects of buildings. Multi-Science; 2006.
[39] Sardo JA. Theory and measurements on H-Darrieus turbines in skewed flow. Tech. Rep. WE-03193. Delft (NL): Delf University of Technology; Aug. 2003.
[40] Ferreira CS, van Bussel G, van Kuik G. Wind tunnel hotwire measurements, flow visualization and thrust measurement of a VAWT in skew. J Sol Energy Eng 2006;128:487–97.
[41] Ferreira CS, Dixon K, Hofemann C, van Kuik G, van Bussel G. The vawt in skew: stereo-PIV and vortex modeling. In: 47th AIAA aerospace sciences meeting including the new horizons forum and aerospace exposition, Orlando, Florida (US); 2009.
[42] Ferreira CS, van Kuik G, van Bussel G. An analytical method to predict the variation in performance of an H-Darrieus in skewed flow and its experimental validation. In: European wind energy conference & exhibition, athens (GR); 2006.
[43] Scheurich F, Brown R. Vertical-axis wind turbines in oblique flow: sensitivity to rotor geometry. In: Ewea 2011 conference, Brussels (be); 2011.
[44] Pedersen T, Paulsen U, Vita L, Madsen H, Nielsen P, Kragh KA, et al. Design and manufacture of an offshore concept wind turbine - the DeepW demonstrator. Tech. Rep. E-0030, DTU Wind Energy. May 2013.
[45] Blackwell B, Reis G. Blade shape for a troposkien type of vertical-axis wind turbine. Tech. Rep. DLA-74–0154. Sandia National Laboratories; Apr. 1974.
[46] Blackwell B, Sheldahl R, Feltz L. Geometrical aspects of the troposkien as applied to the darrieus vertical-axis wind turbine. In: Asme design engineering technical conference, Washington D.C. (US); 1975.
[47] Mercker E, Wiedemann J. On the correction of interference effects in open jet wind tunnels. Tech. Rep. 960671. SAE International; 1996.
[48] V. Dossena, G. Persico, B. Paradiso, L. Battisti, S. Dell'Anna, E. Benini, A. Brighenti, An experimental study of the aerodynamics and performance of a Vertical Axis Wind Turbine in confined and unconfined environment, ASME J Energy Resour Technol 137.
[49] L. Battisti, E. Benini, A. Brighenti, M. Raciti Castelli, S. Dell'Anna, V. Dossena, G. Persico, U. Paulsen, T. Pedersen, Normalized performance and load data for the DeepWind demonstrator in controlled conditions, Energy - Data in Brief - submitted.
[50] I. O. for Standardization, Iso env 13005. Guide to the expression of uncertainty in measurement. Tech. rep.. May 1999.
[51] Ferreira CS, van Bussel G, van Kuik G. An analytical method to predict the variation in performance of a H-Darrieus in skewed flow and its experimental validation. In: Ewec 2006 conference, athens (GR); 2006.
[52] Roh S, Kang S. Effects of a blade profile, the Reyolds number, and the solidity on the performance of a straight bladed vertical axis wind turbine. J Mech Sci Technol 2013;27(11):3299–307.
[53] S. Brusca, R. Lanzafame, M. Messina, Design of a vertical-axis wind turbine: how the aspect ratio affects the turbine's performance, Int J Energy Environ Eng 5 (333–340).
[54] Bogateanu R, Dumitrache A, Dumitrescu H, Stoica CI. Reynolds number effects on the aerodynamic performance of small VAWTs. U.P.B Sci Bull 2014;76(1): 25–36. series D.
[55] Castelli M Raciti, Benini E. Effect of blade thickness on darrieus Vertical-Axis wind turbine performance. In: Proceedings of the 2nd international conference on computer modelling and simulation, Brno (CZ); 2011. p. 110–8. ISBN 978-80-214-4320-4.
[56] Betz A. Applied airfoil theory. Unsymmetrical and non-steady types of motion, Aerodynamic Theory IV. 1935. p. 97–107.
[57] Jones R. Wing theory. Princeton University Press; 1990.